Interface-enhanced helicity dependent photocurrent in metal/semimetal bilayers

Hana Hirose,[1] Masashi Kawaguchi ◉,[1] Yong-Chang Lau ◉,[1,2,3] Zhendong Chi,[1] Frank Freimuth ◉,[4]
Koki Takanashi ◉,[2,3,5] and Masamitsu Hayashi ◉[1]

[1]*Department of Physics, The University of Tokyo, Tokyo 113-0033, Japan*
[2]*Institute for Materials Research, Tohoku University, Sendai 980-8577, Japan*
[3]*Center for Spintronics Research Network, Tohoku University, Sendai 980-8577, Japan*
[4]*Peter Grünberg Institut and Institute for Advanced Simulation, Forschungszentrum Jülich and JARA, 52425 Jülich, Germany*
[5]*Center for Science and Innovation in Spintronics, Core Research Cluster, Tohoku University, Sendai 980-8577, Japan*

One of the hallmarks of light-spin interaction in solids is the appearance of photocurrent that depends on the light helicity. Recent studies have shown that helicity dependent photocurrent (HDP) emerges due to light induced spin current and the inverse spin Hall effect of semimetal thin films. We have studied HDP in metal/semimetal bilayers. Compared to Bi single layer films, we find the HDP is enhanced in metal/Bi bilayers. For the bilayers, the sign of HDP under back illumination reverses from that of front illumination. The back illumination photocurrent is the largest for Ag/Bi bilayers among the bilayers studied. Using a diffusive spin transport model, we show that the HDP sign reversal under back illumination is caused by spin absorption and spin to charge conversion at the interface. Such interfacial effects contribute to the HDP enhancement under front illumination for the bilayers when the Bi layer thickness is small. These results show that the HDP can be used to assess interface states with strong spin orbit coupling.

The exchange of spin angular momentum between electrons plays a fundamental role in modern spintronics as it allows current induced control of magnetism [1]. The concept can be extended to interaction of electron spins with light: the transfer of spin angular momentum from light to electrons allows manipulation of magnetization using ultrashort laser pulses in magnetic thin films [2–4]. The interaction of light with electron spin also manifests itself in photocurrents, i.e., currents that flow when solids are irradiated with light. For example, irradiation of circularly polarized light to materials that possess spin-momentum locked bands results in generation of helicity dependent anisotropic photocurrent. The effect, often referred to as the circularly photogalvanic effect (CPGE), has been identified in semiconductor heterostructures [5,6], topological surface states [7–9], van der Waals structures [10,11] and (semi-)metallic interface states [12,13]. In addition, other forms of photocurrent emerge depending on certain symmetry of the system (e.g., broken structural inversion symmetry and/or broken time reversal symmetry) [14–18].

Recent studies have shown that helicity dependent photocurrent appears in thin films composed of semimetals (e.g., Bi, doped Bi alloys) [19]. The effect has been described assuming that circularly polarized light induces spin density, i.e., an imbalance in the population of carriers with spin parallel and antiparallel to the light spin angular momentum, via the inverse Faraday effect (IFE) [20–26]. Due to the finite penetration depth of the light intensity, a gradient in the spin density develops, which causes flow of spin current along the film normal. The spin current is converted to charge current via the inverse spin Hall effect (ISHE) [27] of Bi. This pro-

cess is sketched in Fig. 1(a), which we refer to as the bulk contribution to the helicity dependent photocurrent.

Here we study helicity dependent photocurrent (HDP) in metal/Bi bilayers. The HDP is found to be larger for Ag/Bi bilayer compared to Bi single layer films. Front and back light illuminations are used to separate contributions from the bulk and those associated with interface states, if any. Illustration of the process is described in Fig. 1. For the bulk contribution [19], the sign of HDP will be the same for front and back illuminations since the direction of spin current, j_s in Figs. 1(a) and 1(b), is the same. In contrast, the spin direction of the electrons present at the bottom surface of Bi (or the metal/Bi interface for metal/Bi bilayers [Figs. 1(c), 1(d)]) is opposite for the front and back illuminations. Under such circumstance, interfacial effects (e.g., spin absorption, the inverse Rashba-Edelstein effect (IREE) [28]) can cause current that flows in opposite direction for the two geometries: compare Figs. 1(c) and 1(d). Thus the photocurrent measurements using front and back illuminations allow one to separate bulk and interfacial contributions. We find that the sign of photocurrent reverses for front and back illuminations in Cu/Bi and Ag/Bi bilayers. The magnitude of the photocurrent under back illumination is the largest for Ag/Bi bilayers, indicating that the degree of spin absorption and spin to charge conversion at the interface is the largest.

Metal/Bi bilayers are deposited on quartz crystal substrates using RF magnetron sputtering. The film structure is sub./seed/t Bi/2 MgO/1 Ta (thickness in nm). We refer to films with and without the seed layer as seed/Bi bilayer and Bi single layer, respectively. The seed layer for the bilayers is
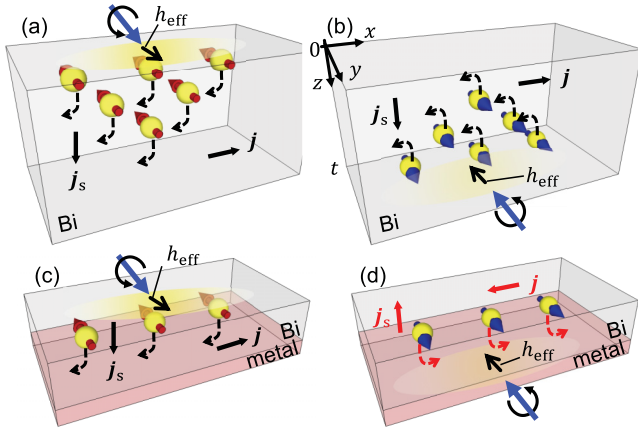
FIG. 1. (a)–(d) Schematic illustrations depicting light induced spin density via the IFE when the film is irradiated with a right-handed circularly polarized light from front (a),(c) and back (b),(d). See Fig. 2(a) for the geometry of front and back illuminations. h_{eff} represents the y component of the effective magnetic field associated with circularly polarized light. Gradient in the spin density, caused by the finite light penetration depth, generates a spin current (j_s) along the film normal. Spin current is converted to charge current (j) via the ISHE. The direction to which j_s flows is the same for front and back illuminations for Bi single layer (a),(b). When a spin absorbing interface is present in metal/Bi bilayer (c),(d), spin current flows toward the interface.

0.5 Ta/2 Cu, 0.5 Ta/2 Ag, 2 W and 0.5 Ta/2 Pt (thickness in nm). The 0.5-nm-thick Ta layer is deposited before the seed layer to promote its smooth growth. The 2 MgO/1 Ta layers serve as a capping layer. Wires are formed by inserting a metal shadow mask between the substrate and the sputtering target during the deposition process [12].

The experimental setup and definition of the coordinate axis are described in Fig. 2(a). The wire is irradiated with light from an oblique angle ($\sim 45°$). We refer to front and back illuminations when the wire is irradiated with light from the film side or from the back of the substrate, respectively. The light plane of incidence is always orthogonal to the wire's long axis. A continuous wave semiconductor laser with wavelength λ and power P is used as the light source. Typical results from
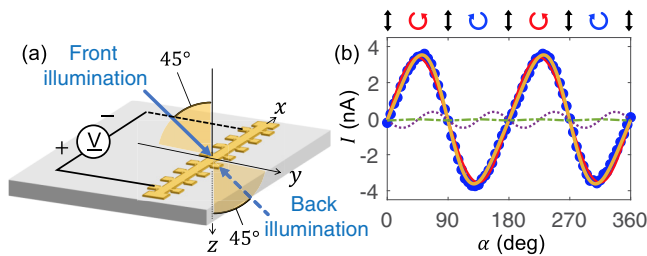

FIG. 2. (a) Schematic illustration of the experimental setup. The yellow caterpillar like structure represents the wire made of the film. Definition of front and back illuminations are sketched. (b) The α dependence of the photocurrent (I) for Ag/Bi bilayer film with $t \sim 65$ nm. The orange solid line shows fit to the data with Eq. (1). The red solid, purple dotted and green dashed lines show contributions from the C, L_1, and L_2 terms, respectively.
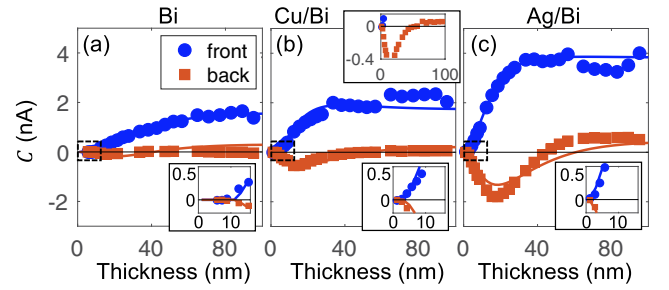

FIG. 3. (a)–(c) Bi layer thickness (t) dependence of the HDP (C) under front (blue circles) and back (orange squares) illuminations for Bi single layer (a), Cu/Bi bilayer (b), Ag/Bi bilayers (c). The solid lines show calculated C using the model. The lower insets show a magnified view of the region marked by the dashed black box. The upper inset to (b) shows that C under back illumination changes sign at $t \sim 50$ nm.

$\lambda = 405$ nm and $P \sim 2.5$ mW are presented. The laser spot size is ~ 0.5 mm in diameter. The photovoltage of the wire (width: $w \sim 0.4$ mm, length: $L \sim 7$ mm) is measured while passing light through a quarter wave plate. The angle (α) of the quarter wave plate's optical axis with respect to the light plane of incidence defines the light helicity: the light is linearly polarized when $\alpha = 0°, 90°, 180°, 270°$ and circularly polarized when $\alpha = 45°, 225°$ (left handed) and $135°, 315°$ (right handed). The photovoltage is converted to photocurrent by dividing the voltage with the resistance of the wire inside the laser spot (~ 0.5 mm long).

Figure 2(b) shows the α dependence of the photocurrent from a Ag/Bi bilayer under front illumination. The data is fitted to the following function to extract parameters with different symmetries:

$$I = C \sin 2(\alpha + \alpha_0) + L_1 \sin 4(\alpha + \alpha_0)$$
$$+ L_2 \cos 4(\alpha + \alpha_0) + I_0, \quad (1)$$

C represents photocurrent that depends on the helicity of light, whereas L_1 and L_2 reflect photocurrent that differ for circularly and linearly polarized light [7,8]. I_0 corresponds to an offset photocurrent that does not depend on α and α_0 is an offset angle associated with the experimental setup (here $\alpha_0 \sim 1°$). The fitted curve is shown by the orange solid line in Fig. 2(b), which agrees well with the data. [Data from all samples can be described with Eq. (1)]. As evident, the photocurrent is dominated by the helicity dependent term (C): the other contributions (L_1, L_2, and I_0) are typically smaller than C; see Appendix A 1 and Fig. 5.

The Bi layer thickness dependence of C for Bi single layer, Cu/Bi and Ag/Bi bilayers using front and back light illuminations are shown in Figs. 3(a)–3(c). For front illumination, all structures show an increase in C with increasing Bi layer thickness (t) until it saturates. The saturation value of C is the largest for the Ag/Bi bilayer and is the smallest for Bi single layer. Note that C upon saturation for the Cu/Bi bilayers is nearly an order of magnitude larger than that reported previously [12]. In the lower insets to Figs. 3(a)–3(c), we show a magnified view of the region marked by the dashed black box. We find that the minimum thickness (t_d) at which

C takes a non-negligible value depends on the film structure. In particular, t_d is close to 10 nm for Bi single layer films. We infer that the Bi layer within this thickness ($t < t_d$) do not contribute to the generation of light induced spin density, thus forming a spin excitation dead layer possibly due to the different structure/texture of Bi.

For back illumination, C is nearly zero for Bi single layer in the entire thickness range studied. If t_d is close to or larger than the light penetration depth, light entering from the back of the substrate will not reach a region where a nonzero spin density can be induced, resulting in near zero C for back illumination. In contrast, for Cu/Bi and Ag/Bi bilayers under back illumination, a large negative C is found when t is small. C increases with increasing t and changes its sign from negative to positive when $t \sim 40$ nm. (For the Cu/Bi bilayers, the upper inset to Fig. 3(b) shows the sign change). These results indicate that, in Cu/Bi and Ag/Bi bilayers, there are two sources of photocurrents with opposite signs that contribute to C. Note that t_d is slightly larger for the Cu/Bi bilayers compared to that of the Ag/Bi bilayers; see the lower insets of Figs. 3(b) and 3(c). In addition, the metallic seed layer reduces the light amplitude that enters the Bi layer by more than 20% for back illumination (see Appendix A 2 for the details). These effects reduce the overall signal of C and cause a nearly zero C for back illuminated Cu/Bi bilayer with large t.

To model the system, we solve the spin diffusion equation with a source term associated with light induced spin density. We first define the source term. The number of photons absorbed in Bi at position z is defined as $n_{ph}(z)$: $z = 0$ corresponds to the top surface of the Bi layer in contact with the MgO/Ta capping layer; see Fig. 1(b). We assume the following simplified functional form for $n_{ph}(z)$:

$$n_{ph}(z) = A \exp\left(-\alpha_{eff} z\right). \tag{2}$$

(For back illumination, substitute $(t - z)$ for z.) α_{eff} is the effective extinction constant and A is a coefficient representing the light amplitude for a given Bi layer thickness t. In the absence of multiple reflections within the film, A is a constant and equals the power of the incident light. Here we take into account multiple reflections and thus A depends on t.

To obtain A and α_{eff}, we measure the reflectivity R and transmittance T of circularly polarized light with which the films are irradiated. The measured R and T for both front and back illuminations for Bi single layer, Cu/Bi and Ag/Bi bilayers are shown in Appendix Fig. 7. Taking into account multiple reflections that take place at the substrate/film and film/air interfaces (see Appendix A 2 and Fig. 6), we fit the thickness dependence of R and T to estimate the refractive index n and extinction coefficient κ of the films. The estimated values of n and κ are shown in Table I, which are in good agreement with past report on bulk Bi [29].

The absorbance (P_a) of a film is expressed as

$$P_a = P(1 - R - T), \tag{3}$$

where P is the light power incident on the film. We equate P_a divided by the energy of one photon $\frac{hc}{\lambda}$ (c is the speed of light, h is the Planck constant) and the area of a laser spot S with the

TABLE I. Parameters used in the model calculations. The spin diffusion equation [Eq. (6)] is solved to obtain the spin current density j_s, which is substituted in Eq. (10) to calculate j_c, from which the total charge current $I_{c,x}$, equivalent to C, is obtained. ξ, λ_s, l_{int} and t_d are adjusted to fit the experimental data. n and κ are obtained from the reflectivity and transmittance measurements (the results are shown in Fig. 7).

Structure	ξ	λ_s (nm)	n	κ	l_{int} (nm)	t_d (nm)
Bi single layer	0.7	18	1.3	3.2	N/A	12
Cu/Bi bilayer	0.7	18	1.3	3.0	6	4
Ag/Bi bilayer	1.4	18	1.3	2.5	3	1

thickness integrated sum of $n_{ph}(z)$, i.e.,

$$P_a\left(\frac{hc}{\lambda}\right)^{-1}\frac{1}{S} = \int_0^t n_{ph}(z)dz$$
$$= \int_0^t A \exp\left(-\alpha_{eff} z\right)dz. \tag{4}$$

Using Eqs. (3) and (4) and R and T calculated using the experimentally obtained n and κ [see Appendix Eqs. (A4) and (A6) for the relation between R, T and n, κ], we estimate A for each t. We assume $\alpha_{eff} = \frac{4\pi\kappa}{\lambda}$ for all samples. Substituting A and α_{eff} into Eq. (2), we obtain the number of photons [$n_{ph}(z)$] absorbed at z for a given film thickness t. For simplicity, we assume one photon absorbed at position z in the film generates spin density equivalent of $\frac{\hbar}{2}$ ($\hbar = h/(2\pi)$). Defining n_s as the number of electrons that are spin polarized along the light spin angular momentum, i.e., the spin density, we obtain

$$n_s(z) = n_{ph}(z). \tag{5}$$

We use $n_s(z)$ as the source term of the spin diffusion equation.

The spin diffusion equation is expressed using the chemical potential difference (μ_s) of the electrons with spin pointing parallel and antiparallel to the light spin angular momentum, that is,

$$\frac{\partial^2 \mu_s(z)}{\partial z^2} = \frac{1}{\lambda_s^2}\mu_s(z) + \frac{e^2}{\sigma_{xx}}n_s(z), \tag{6}$$

where λ_s is the spin diffusion length and σ_{xx} is the conductivity of Bi ($\sigma_{xx} \sim 1 \times 10^5$ $(\Omega \cdot m)^{-1}$). Note that λ_s includes information of spin relaxation. We solve Eq. (6) to obtain $\mu_s(z)$, which can be converted to spin current density (j_s) via the relation,

$$j_s(z) = -\frac{\sigma_{xx}}{2e}\nabla\mu_s(z) \tag{7}$$

$j_{s,i}$ represents spin current along the i direction with polarization pointing along the light spin angular momentum, which we represent by a unit vector e_σ. The boundary condition is defined as

$$j_{s,z}(z = 0) = 0, \quad j_{s,z}(z = t) = 0, \tag{8}$$

for Bi single layer and

$$j_{s,z}(z = 0) = 0, \quad j_{s,z}(z = t) = -\frac{\sigma_{xx}}{2e}\frac{\mu(z = t)}{l_{int}}, \tag{9}$$
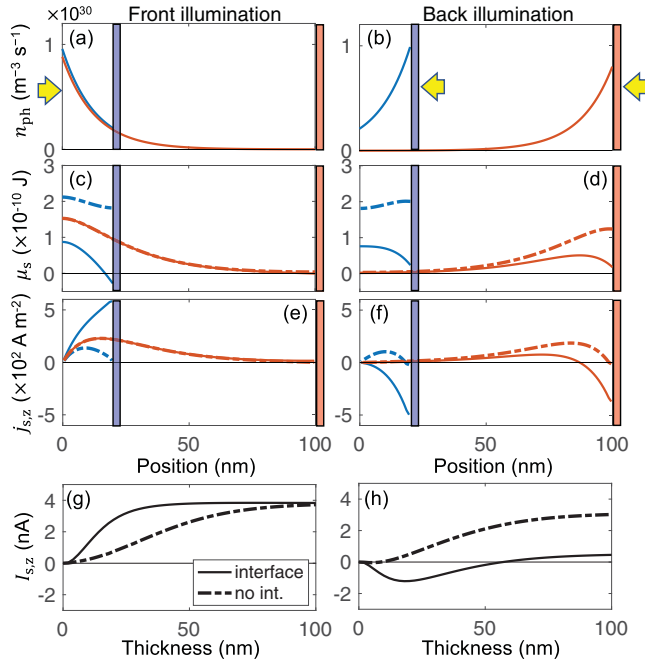
FIG. 4. (a)–(f) Number of absorbed photons (n_{ph}) (a),(b), chemical potential difference (μ_s) of the electrons with spin pointing parallel and antiparallel to the light spin angular momentum (c),(d), and the spin current density ($j_{s,z}$) along z (e), (f), plotted against film position z for front (a), (c), (e) and back (b), (d), (f) illuminations. The blue and red lines show results when the film thickness (t) is 20 nm and 100 nm, respectively. The red and blue thick vertical lines indicate the position of metal/Bi interface and the yellow arrow represents the direction from which light enters. $z = 0$ (the horizontal axis origin) corresponds to the top interface of the Bi layer (in contact with the MgO/Ta capping layer). (g), (h) t dependence of the z component of the thickness integrated spin current ($I_{s,z} = w \int_0^t j_{s,z}(z)dz$) for front (g) and back (h) illuminations. (a)–(h) The solid and dashed lines represent calculation results when a spin absorbing interface is present and absent, respectively. The parameters used are the same with those of Ag/Bi bilayers described in Table I.

for the seed/Bi bilayers. The seed/Bi interface at $z = t$ is assumed to absorb spin current. The degree of absorbance is characterized by l_{int} [28]. Note that this boundary condition does not explicitly include contributions from, for example, the IREE: it simply describes the presence of an interface that varies the spin current boundary condition. Finally, the ISHE converts the spin current to charge current density ($\boldsymbol{j}_c$):

$$\boldsymbol{j}_c(z) = \xi \boldsymbol{j}_s(z) \times \boldsymbol{e}_\sigma, \tag{10}$$

where ξ is the charge to spin interconversion efficiency. ξ is related to the spin Hall angle θ_{SH} via $\xi = \tan(\theta_{SH})$. The total charge current along x ($I_{c,x}$), which is measured experimentally, is obtained by integrating the x component of $\boldsymbol{j}_c$ over z and multiplying $\sin(\pi/4)$ (to account for the oblique incidence of light) and the width of the wire.

Figures 4(a)–4(f) show the calculated $n_{ph}(z)$, $\mu_s(z)$ and $j_{s,z}(z)$ for films with thickness $t = 20$ nm (blue lines) and $t = 100$ nm (red lines) under front and back illuminations. The solid and dashed lines show results with ($\frac{1}{l_{int}} \neq 0$) and without ($\frac{1}{l_{int}} = 0$) a spin absorbing interface, respectively. The

difference of the maximum n_{ph} among all conditions shown in Figs. 4(a) and 4(b) is due to multiple reflections within Bi. The profiles of μ_s and $j_{s,z}$ significantly change when a spin absorbing interface is present.

The spin current integrated across the Bi layer thickness, $I_{s,z} = w \int_0^t j_{s,z}(z)dz$, is plotted as a function of t in Figs. 4(g) and 4(h). Without the interface (dashed lines), $I_{s,z}$ increases with increasing t until saturation and is positive for front and back illuminations. With the interface (solid lines), however, the signs of $I_{s,z}$ for front and back illuminations are opposite when t is small. $I_{s,z}$ for back illumination is negative for small t and changes its sign at a $t \sim 50$ nm. As evident in Fig. 4(f) [see also Fig. 1(d) for a schematic illustration], the presence of spin absorbing interface induces spin current toward the interface. For films with small t, $I_{s,z}$ is dominated by such back flow toward the interface. In addition, $I_{s,z}$ for front illumination with the spin absorbing interface is larger compared to that without the interface when t is small.

With this model, we calculate the total charge current $I_{c,x}$, equivalent to C, that matches the experimental data by adjusting ξ, λ_s, l_{int} and t_d. t_d is estimated from the minimum Bi layer thickness at which a non-negligible C is observed (see the lower insets of Fig. 3). For Bi single layer, $1/l_{int}$ is set to zero. The optical constants (n and κ) are obtained from the reflectivity and transmittance measurements described in Appendix A 3. The calculated C, presented by the blue and orange solid lines in Figs. 3(a)–3(c), show good agreement with the experimental results. The parameters used for the calculations are listed in Table I.

ξ of Bi obtained here is considerably larger than that of previous reports estimated using spin pumping measurements [30,31], but is in relatively good agreement with that of sputtered Bi-rich BiSb alloys [32]. The estimated ξ of Ag/Bi bilayers is nearly twice as large as that of other structures. Note that the resistivity of Bi for the structures studied is similar. Spin-torque ferromagnetic resonance (ST-FMR) measurements are carried out in heterostructures that contain Bi and a ferromagnetic layer (CoFeB). See Appendix A 5 for the details of the experimental setup and the results. We find that ξ of Bi, Cu/Bi and Ag/Bi estimated using ST-FMR roughly agrees with that presented in Table I.

In the model, we assume the interface modifies the spin current profile in Bi via changes in the boundary condition. The IREE [28,33,34] can convert the spin current that flows into the interface to generate a charge current, providing an additional channel. Interestingly, the size of l_{int} required to describe the results for Ag/Bi bilayers is close to that reported in similar systems [28]. With the current model, however, it is difficult to separate contributions from the ISHE and IREE.

We have also studied photocurrent in W/Bi and Pt/Bi bilayers, in which the seed layer exhibits significantly larger spin Hall effect than Cu and Ag [35,36]; see Appendix Fig. 8. We find that C is not particularly large for these bilayers compared to that of Cu/Bi and Ag/Bi bilayers. As the carrier density of Bi is more than three orders of magnitude smaller than that of typical metals (W and Pt) [19], we consider spin current flowing into the seed layer (and the 0.5-nm-thick Ta underlayer), if any, hardly contributes to the charge current within the seed layer via the ISHE [37]. Inverted structures, e.g., Bi/W and Bi/Pt bilayers, have also been studied. In

these structures, we find the overall sign and magnitude of C for front illumination is the same as in the normal structures (W/Bi and Pt/Bi bilayers). These results support the notion that the dominant contribution to the HDP originates from the bulk of Bi and not from the metallic layers.

Finally, we discuss contributions from the CPGE. Note that CPGE does not require injection of spin current into the interface, which is different from IREE. If CPGE is the source of C for the seed/Bi bilayers, we expect a constant C for back illumination and an opposite sign C that decays with film thickness (when t exceeds $1/\alpha_{eff}$) for front illumination. From the Bi layer thickness dependence of C, however, it seems as if contribution from the CPGE is rather small. Given that there are several mechanisms that contribute to the HDP, it is difficult to assess the size of CPGE in this system.

In summary, we have studied bulk and interface contributions to the helicity dependent photocurrent (HDP) in metal/Bi bilayers. As reported previously, the bulk contribution originates from the ISHE of Bi, which converts light induced spin current to charge current within Bi. In metal/Bi bilayers, we find that not only the HDP increases under front illumination, compared to Bi single layer, but also the sign of HDP reverses for back illumination. Using a diffusive spin transport model, we show that the metal/Bi interface acts as a strong spin sink and modifies the profile of spin current in Bi. Such change in the spin current profile results in an enhancement of HDP due to the ISHE of Bi as well as the IREE at the interface. We find the largest HDP in Ag/Bi bilayers, both under front and back illuminations, suggesting strong contributions from the interface. These results thus demonstrate means to study spin absorption and spin to charge conversion at interfaces using circularly polarized light. Given that the photocurrent in metal/Bi bilayers is dominated by the helicity dependent component, the large HDP found here can be exploited for polarization sensitive detectors in optical communications [38] as well as light spin angular momentum detectors for quantum optics [39].

APPENDIX

1. Helicity and polarization dependent photocurrent

Components of the photocurrent, L_1, L_2, and I_0, obtained by fitting the data (I vs α) with Eq. (1), are shown in Fig. 5 as a function of Bi layer thickness (t) for Bi single layer,
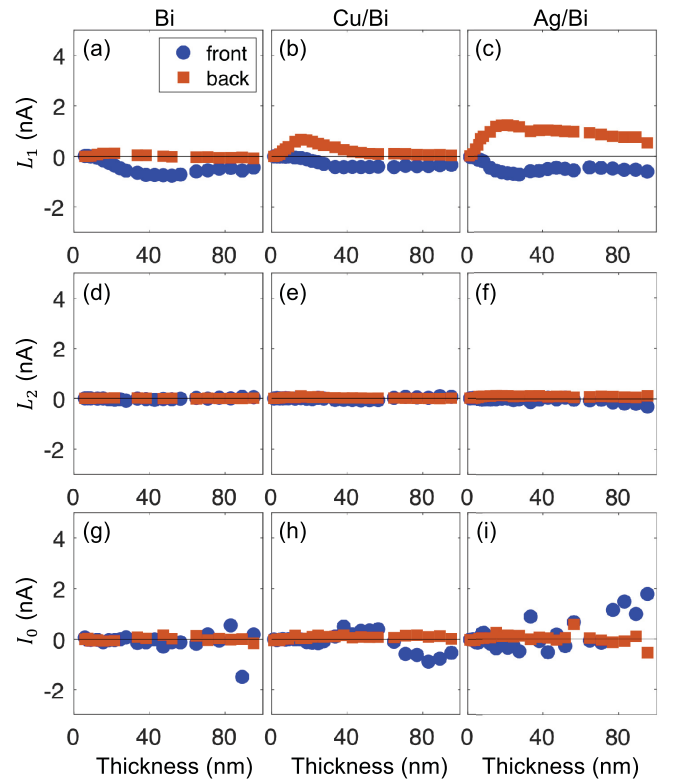

FIG. 5. (a)–(i) Bi layer thickness (t) dependence of the photocurrent components, L_1 (a), (b), (c), L_2 (d), (e), (f) and I_0 (g), (h), (i), obtained by fitting the data with Eq. (1). The results show photocurrent from Bi single layer (a), (d), (g), Cu/Bi bilayer (b), (e), (h) and Ag/Bi bilayer (c), (f), (i). Blue circles and orange squares represent results under front and back illuminations, respectively.

Cu/Bi and Ag/Bi bilayers. In all cases, C (see Fig. 3) and L_1 show a similar thickness dependence, suggesting that the two effects have a common origin. L_2 and I_0 are negligible in all structures. For the thicker Bi films, I_0 shows relatively large fluctuation, which we consider is related to laser induced heating effects that may originate from the large thermoelectric effects of Bi.

2. Multiple reflection model and absorption of light

We calculate the reflectivity R and transmittance T of the system assuming that multiple reflections take place at the top and bottom interfaces of the semimetal (Bi) layer. We model the system using three media: air (medium 1), the film including the seed and capping layers (medium 2), and the quartz substrate (medium 3). Since the seed layer and the capping layer are thin compared to the light wavelength, we include them as part of the Bi layer. Note that the Cu and Ag seed layers reduce the amplitude of light transmission. We have measured the light transmission probability (T_{seed}) of a 0.5 Ta/2 Cu deposited on quartz crystal and found $T_{seed} \sim 0.76$. We assume 0.5 Ta/2 Ag possesses similar T_{seed}.

The refractive index of the three media is defined as $n_1 = 1.0 + i0$ (air), $n_2 = n + i\kappa$ (film) and $n_3 = 1.5 + i0$ (substrate). The thickness of the film is d_2. Transmission loss of the substrate is studied separately using a substrate without
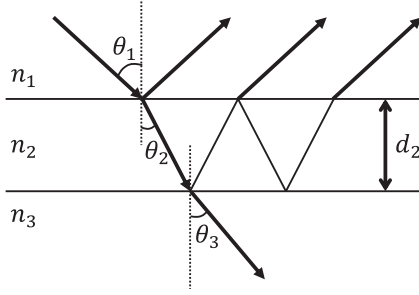
FIG. 6. Schematic illustration of the model system. Multiple reflections take place within the film.

the film. The transmission probability is $T_{sub}^s \sim 0.908$ for s-polarized light and $T_{sub}^p \sim 0.991$ for p-polarized light. The film is irradiated with light from an oblique angle of $45°$. Schematic illustration of the system is shown in Fig. 6.

When a $s(p)$-polarized light with wavelength λ is incident from medium 1 (air) with an oblique angle θ_1 on medium 2 (film), the amplitude of the reflected light ($r_{123}^{s(p)}$) and the transmitted light ($t_{123}^{s(p)}$) are

$$r_{123}^{s(p)} = \frac{r_{23}^{s(p)} + r_{12}^{s(p)} \exp(i\gamma)}{1 + r_{23}^{s(p)} r_{12}^{s(p)} \exp(i\gamma)},$$

$$t_{123}^{s(p)} = \frac{t_{23}^{s(p)} t_{12}^{s(p)} \exp(i\gamma/2)}{1 + r_{23}^{s(p)} r_{12}^{s(p)} \exp(i\gamma)}. \quad (A1)$$

$r_{ij}^{s(p)}$ and $t_{ij}^{s(p)}$ are the Fresnel reflection and transmission coefficients for $s(p)$-polarized light, defined as

$$r_{ij}^s = \frac{n_i \cos\theta_i - n_j \cos\theta_j}{n_i \cos\theta_i + n_j \cos\theta_j},$$

$$t_{ij}^s = \frac{2n_i \cos\theta_i}{n_i \cos\theta_i + n_j \cos\theta_j},$$

$$r_{ij}^p = \frac{n_j \cos\theta_i - n_i \cos\theta_j}{n_j \cos\theta_i + n_i \cos\theta_j},$$

$$t_{ij}^p = \frac{2n_i \cos\theta_i}{n_j \cos\theta_i + n_i \cos\theta_j}. \quad (A2)$$

In Eq. (A1), $\gamma \equiv \frac{4\pi}{\lambda} n_2 d_2 \cos\theta_2$, where θ_2 is the complex refraction angle in the film. The reflection ($R_{123}^{s(p)}$) and transmission ($T_{123}^{s(p)}$) probabilities of the $s(p)$-polarized light are written as

$$R_{123}^{s(p)} = \left| r_{123}^{s(p)} \right|^2,$$

$$T_{123}^{s(p)} = \left| \frac{n_3 \cos\theta_3}{n_1 \cos\theta_1} \right| \left| t_{123}^{s(p)} \right|^2, \quad (A3)$$

where θ_3 is the complex refraction angle of the transmitted light in medium 3.

The reflection R_{123}^c and transmission T_{123}^c probabilities of a circularly polarized light are expressed as

$$R_{123}^c = \frac{1}{2}\left(R_{123}^s + R_{123}^p\right),$$

$$T_{123}^c = \frac{1}{2}\left(T_{123}^s T_{sub}^s + T_{123}^p T_{sub}^p\right)T_{seed}. \quad (A4)$$
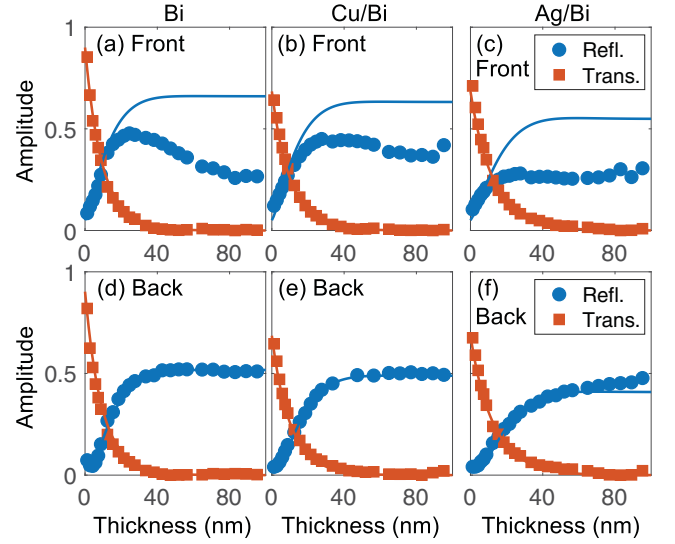

FIG. 7. (a)–(f) Reflectivity R (solid circles) and transmittance T (solid squares) of left-handed circularly polarized light under front illumination (upper panels) and back illumination (lower panels) for Bi single layer (a,d), Cu/Bi bilayer (b,e) and Ag/Bi bilayer (c,f), plotted as a function of t. Solid lines show the calculated values of R and T that best fit the experimental results.

The absorbance of the film for circularly polarized light is calculated as

$$A_{123}^c = \frac{1}{2}\left(\left\{1 - \left(R_{123}^s + T_{123}^s\right)\right\} + \left\{1 - \left(R_{123}^p + T_{123}^p\right)\right\}\right). \quad (A5)$$

For back illumination, we exchange parameters of medium 1 with those of medium 3. One needs to replace Eqs. (A4) and (A5) with the following relations:

$$R_{123}^c = \frac{1}{2}\left(\left(T_{sub}^s\right)^2 R_{123}^s + \left(T_{sub}^p\right)^2 R_{123}^p\right) \text{ [back illumination]},$$

$$T_{123}^c = \frac{1}{2}\left(T_{123}^s T_{sub}^s + T_{123}^p T_{sub}^p\right)T_{seed} \text{ [back illumination]}, \quad (A6)$$

$$A_{123}^c = \frac{1}{2}\left(T_{seed} T_{sub}^s \left\{1 - \left(R_{123}^s + T_{123}^s\right)\right\} + T_{seed} T_{sub}^p \left\{1 - \left(R_{123}^p + T_{123}^p\right)\right\}\right) \text{ [back illumination]}. \quad (A7)$$

3. Measurements of the optical constants

The optical constants of the films are estimated from measurements of the reflectivity (R) and transmittance (T) of circularly polarized light. The measured R and T for front and back illuminations for Bi single layer, Cu/Bi and Ag/Bi bilayers are shown by the symbols in Figs. 7(a)–7(c) and 7(d)–7(f), respectively. The t dependence of R and T are fitted with Eqs. (A4) and (A6) to extract n and κ of the film. The extracted values are listed in Table I. The absorbance are calculated using Eqs. (A5) and (A7). A_{123}^c is equivalent to P_a in Eq. (4).
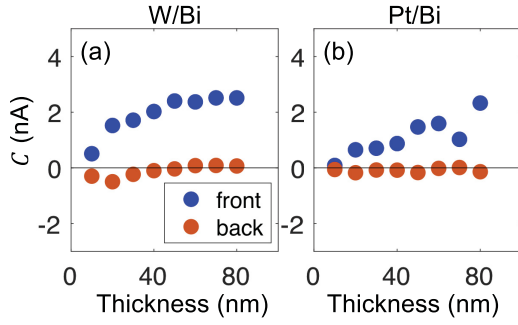
FIG. 8. (a), (b) Bi layer thickness (t) dependence of the HDP (C) under front (blue circles) and back (orange squares) illuminations for W/Bi (a) and Pt/Bi bilayers (b).

4. Helicity dependent photocurrent for W/Bi and Pt/Bi bilayers

The t dependence of C for W/Bi and Pt/Bi bilayers are shown in Fig. 8.

5. Spin-torque ferromagnetic resonance measurements

Spin-torque ferromagnetic resonance (ST-FMR) measurements [40] are conducted to quantify the charge to spin interconversion efficiency. The base structure of the samples consists of sub./seed/t Bi/7 CoFeB/2 MgO/1 Ta, where seed is no seed, 0.5 Ta/2 Cu or 0.5 Ta/2 Ag. We denote the three structures as Bi/CoFeB, Cu/Bi/CoFeB and Ag/Bi/CoFeB heterostructures. t is varied from 0 to 30 nm. Since the measurements exploit the anisotropic magnetoresistance of the CoFeB layer, current shunting into the Bi layer can reduce the signal to noise ratio. The maximum thickness of the Bi layer is thus limited to ~30 nm. The thickness of the CoFeB layer is fixed to 7 nm, which reduces parasitic contributions to the spectral line shape including resonant heating at larger CoFeB thicknesses [41] and field-like spin-orbit torque when CoFeB is thin [42].

Films are patterned, using standard optical lithography and Ar ion milling, into microstrips with a nominal length of $L = 40\,\mu$m and a width of $w = 10\,\mu$m. A standard liftoff process is used to pattern the electrodes. For the measurements, an amplitude modulated radio-frequency (RF) microwave with a frequency of f_{RF} and a power of 17 dBm is applied through a ground-signal-ground coplanar waveguide. The amplitude modulation (AM) is set to 25%. An in-plane magnetic field H is applied along an angle ~45° with respect to the long axis of the microstrip. The rectified voltage V_{mix} is measured using a lock-in amplifier synchronized to the AM frequency of 9997 Hz.

Figure 9 shows representative H dependence of V_{mix} for the three structures. A Lorentzian line shape is observed for all structures. From the f_{RF} dependence of the resonance linewidth and the resonance field, we extract the Gilbert damping constant α_G and the effective demagnetizing field $4\pi M_{eff}$ of the CoFeB layer. The t dependence of these quantities are shown in Figs. 10(a) and 10(b). α_G appears to be anticorrelated with $4\pi M_{eff}$, i.e., heterostructures with small α_G typically possesses large $4\pi M_{eff}$ and vice versa.
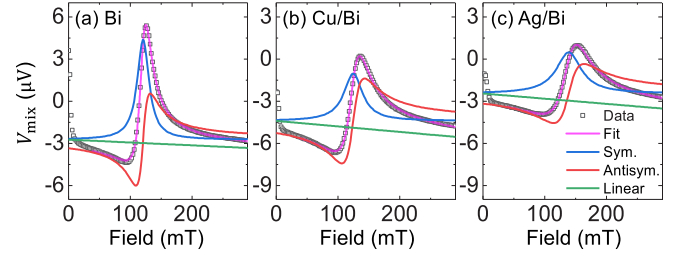

FIG. 9. (a)–(c) The magnetic field dependence of the rectified voltage V_{mix} for Bi/CoFeB (a), Cu/Bi/CoFeB (b) and Ag/Bi/CoFeB (c) heterostructures. The open squares show experimental data, the pink solid lines show fit to the data. The blue, red, and green solid lines show decomposition of the fitted curves into symmetric and antisymmetric Lorentzian, and a linear line, respectively. All data are taken with $f_{RF} = 10$ GHz.

The resonance line shape can be decomposed into the sum of a symmetric and an antisymmetric Lorentzian, which is proportional to the dampinglike effective field and the Oersted field, respectively. In addition, we consider a term that increases linearly with H_{ext}, which accounts for the large ordinary Nernst effect of Bi. The charge to spin interconversion efficiency, denoted as ξ_{FMR}, is obtained using the following relation:

$$\xi_{FMR} = \frac{S}{A}\zeta \frac{e\mu_0 M_s t_{CoFeB} t}{\hbar}\sqrt{1 + \frac{4\pi M_{eff}}{H_{ext}}}, \quad (A8)$$

where S and A are the amplitude of the symmetric and antisymmetric components of the Lorentzian line shape, and t_{CoFeB} is the CoFeB thickness. $\zeta \equiv 1 + \frac{t_{seed}\rho_{Bi}}{t\rho_{seed}}$ is the correction factor for current shunting into the seed layer. t_{seed} and ρ_{seed} are the thickness and the resistivity of the seed layer, and ρ_{Bi} is the resistivity of Bi. For Bi/CoFeB, $\zeta = 1$: We recover the formula derived by Liu *et al.* [40]. For finite t_{seed}, $\zeta > 1$ which indicates that neglecting current shunting into the seed layer leads to an underestimation of the actual spin interconversion efficiency.

To study current distribution in the heterostructures, the sheet conductance σ_s of the samples are measured. σ_s is plotted against t in Fig. 10(c). Within a parallel circuit model, the slope of the linear fit to this plot corresponds to the conductivity of the thickness varying layer (here Bi), provided that varying the thickness of one layer does not affect the conductivity of the other layers. However, none of the heterostructures show such a linear thickness dependence, suggesting that such assumption does not hold. For the Cu/Bi/CoFeB and Ag/Bi/CoFeB heterostructures, σ_s decreases with increasing t. We infer that increasing t leads to increased roughness of the Bi layer, causing an increase in the resistivity of the CoFeB layer.

S and A are plotted against t in Figs. 10(d) and 10(e). Assuming $\rho_{Bi} \sim 1200\,\mu\Omega$ cm, $\rho_{Cu} \sim 50\,\mu\Omega$ cm and $\rho_{Ag} \sim 55\,\mu\Omega$ cm, which can account for the t dependence of σ_s with a t varying resistivity of CoFeB, we apply Eq. (A8) to extract ξ_{FMR}. The t dependence of ξ_{FMR} is plotted in Fig. 10(f). In the limit of large t, we obtain ξ_{FMR} of ~1, ~1.8 and ~2.2 for the Bi/CoFeB, Cu/Bi/CoFeB and Ag/Bi/CoFeB heterostructures. Although the current distribution estimation
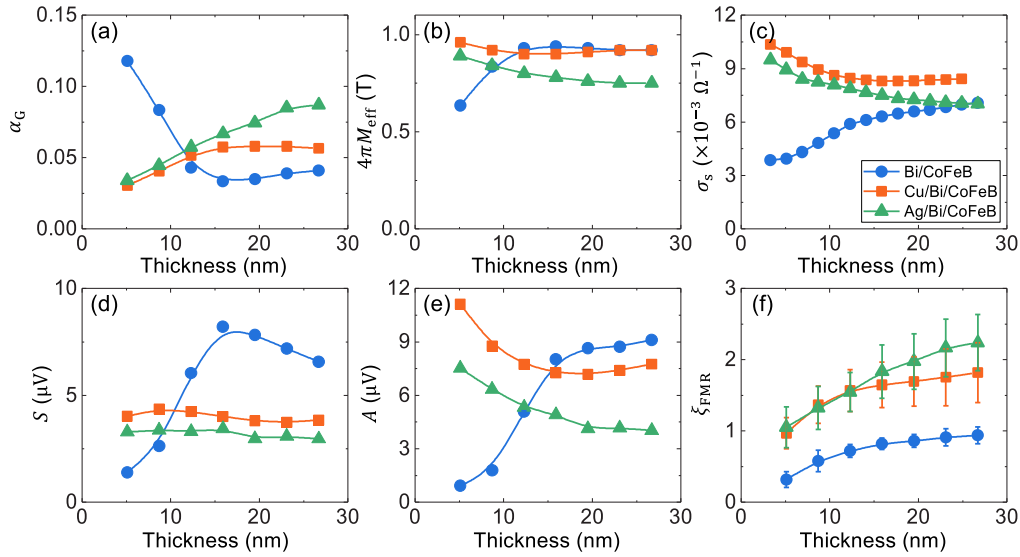
FIG. 10. (a)–(f) Bi layer thickness (t) dependence of the Gilbert damping constant α_G (a) and the effective demagnetizing field $4\pi M_{eff}$ (b) of the CoFeB layer in the heterostructures, the sheet conductance σ_s (c), the amplitude of the symmetric S (d) and antisymmetric A (e) components of the Lorentzian line shape, and the charge to spin interconversion efficiency ξ_{FMR} (f) of the heterostructures. Blue circles, orange squares, and green triangles represent data from Bi/CoFeB, Cu/Bi/CoFeB, and Ag/Bi/CoFeB heterostructures, respectively. The lines are guides to the eye.

within the heterostructures strongly influences the evaluation of ξ_{FMR}, using reasonable values of ρ_{Bi} for all the structures, we typically find ξ_{FMR} for samples with large t in the same order as ξ shown in Table I.

[1] A. Manchon, J. Zelezny, I. M. Miron, T. Jungwirth, J. Sinova, A. Thiaville, K. Garello, and P. Gambardella, Current-induced spin-orbit torques in ferromagnetic and antiferromagnetic systems, Rev. Mod. Phys. **91**, 035004 (2019).

[2] A. V. Kimel, A. Kirilyuk, P. A. Usachev, R. V. Pisarev, A. M. Balbashov, and T. Rasing, Ultrafast non-thermal control of magnetization by instantaneous photomagnetic pulses, Nature (London) **435**, 655 (2005).

[3] C. D. Stanciu, F. Hansteen, A. V. Kimel, A. Kirilyuk, A. Tsukamoto, A. Itoh, and T. Rasing, All-Optical Magnetic Recording with Circularly Polarized Light, Phys. Rev. Lett. **99**, 047601 (2007).

[4] C. H. Lambert, S. Mangin, Bsdcs Varaprasad, Y. K. Takahashi, M. Hehn, M. Cinchetti, G. Malinowski, K. Hono, Y. Fainman, M. Aeschlimann, and E. E. Fullerton, All-optical control of ferromagnetic thin films and nanostructures, Science **345**, 1337 (2014).

[5] S. D. Ganichev, E. L. Ivchenko, V. V. Bel'kov, S. A. Tarasenko, M. Sollinger, D. Weiss, W. Wegscheider, and W. Prettl, Spin-galvanic effect, Nature (London) **417**, 153 (2002).

[6] S. D. Ganichev, V. V. Bel'kov, L. E. Golub, E. L. Ivchenko, P. Schneider, S. Giglberger, J. Eroms, J. De Boeck, G. Borghs, W. Wegscheider, D. Weiss, and W. Prettl, Experimental Separation of Rashba and Dresselhaus Spin Splittings in Semiconductor Quantum Wells, Phys. Rev. Lett. **92**, 256601 (2004).

[7] J. W. McIver, D. Hsieh, H. Steinberg, P. Jarillo-Herrero, and N. Gedik, Control over topological insulator photocurrents with light polarization, Nat. Nanotechnol. **7**, 96 (2012).

[8] K. N. Okada, N. Ogawa, R. Yoshimi, A. Tsukazaki, K. S. Takahashi, M. Kawasaki, and Y. Tokura, Enhanced photogalvanic current in topological insulators via fermi energy tuning, Phys. Rev. B **93**, 081403(R) (2016).

[9] Y. Pan, Q. Z. Wang, A. L. Yeats, T. Pillsbury, T. C. Flanagan, A. Richardella, H. J. Zhang, D. D. Awschalom, C. X. Liu, and N. Samarth, Helicity dependent photocurrent in electrically gated $(Bi_{1-x}Sb_x)_2Te_3$ thin films, Nat. Commun. **8**, 1037 (2017).

[10] H. T. Yuan, X. Q. Wang, B. Lian, H. J. Zhang, X. F. Fang, B. Shen, G. Xu, Y. Xu, S. C. Zhang, H. Y. Hwang, and Y. Cui, Generation and electric control of spin-valley-coupled circular photogalvanic current in WSe_2, Nat. Nanotechnol. **9**, 851 (2014).

[11] Q. Ma, S. Y. Xu, C. K. Chan, C. L. Zhang, G. Q. Chang, Y. X. Lin, W. W. Xie, T. Palacios, H. Lin, S. Jia, P. A. Lee, P. Jarillo-Herrero, and N. Gedik, Direct optical detection of Weyl fermion chirality in a topological semimetal, Nat. Phys. **13**, 842 (2017).

[12] H. Hirose, N. Ito, M. Kawaguchi, Y. C. Lau, and M. Hayashi, Circular photogalvanic effect in Cu/Bi bilayers, Appl. Phys. Lett. **113**, 222404 (2018).

[13] J. Puebla, F. Auvray, N. Yamaguchi, M. R. Xu, S. Z. Bisri, Y. Iwasa, F. Ishii, and Y. Otani, Photoinduced Rashba Spin-To-Charge Conversion Via an Interfacial Unoccupied State, Phys. Rev. Lett. **122**, 256401 (2019).

[14] I. Zutic, J. Fabian, and S. Das Sarma, Spin-Polarized Transport in Inhomogeneous Magnetic Semiconductors: Theory of Magnetic/Nonmagnetic p-n Junctions, Phys. Rev. Lett. **88**, 066603 (2002).

[15] B. Endres, M. Ciorga, M. Schmid, M. Utz, D. Bougeard, D. Weiss, G. Bayreuther, and C. H. Back, Demonstration of the spin solar cell and spin photodiode effect, Nat. Commun. **4**, 2068 (2013).

[16] T. Morimoto and N. Nagaosa, Topological nature of non-linear optical effects in solids, Sci. Adv. **2**, e1501524 (2016).

[17] F. Freimuth, S. Blugel, and Y. Mokrousov, Charge pumping driven by the laser-induced dynamics of the exchange splitting, Phys. Rev. B **95**, 094434 (2017).

[18] R. C. Roca, N. Nishizawa, K. Nishibayashi, and H. Munekata, Investigation of helicity-dependent photocurrent at room temperature from a Fe/x-AlOx/p-GaAs schottky junction with oblique surface illumination, Jpn. J. Appl. Phys. **56**, 04cn05 (2017).

[19] M. Kawaguchi, H. Hirose, Z. Chi, Y.-C. Lau, F. Freimuth, and M. Hayashi, Giant inverse faraday effect in dirac semimetals, (2020), arXiv:2009.01388.

[20] P. S. Pershan, Vanderzi. Jp, and L. D. Malmstrom, Theoretical discussion of the inverse Faraday effect, raman scattering, and related phenomena, Phys. Rev. **143**, 574 (1966).

[21] R. Hertel, Theory of the inverse Faraday effect in metals, J. Magn. Magn. Mater. **303**, L1 (2006).

[22] K. Taguchi and G. Tatara, Theory of inverse Faraday effect in a disordered metal in the terahertz regime, Phys. Rev. B **84**, 174433 (2011).

[23] M. Berritta, R. Mondal, K. Carva, and P. M. Oppeneer, *Ab Initio* Theory of Coherent Laser-Induced Magnetization in Metals, Phys. Rev. Lett. **117**, 137203 (2016).

[24] A. Qaiumzadeh and M. Titov, Theory of light-induced effective magnetic field in rashba ferromagnets, Phys. Rev. B **94**, 014425 (2016).

[25] F. Freimuth, S. Bluegel, and Y. Mokrousov, Laser-induced torques in metallic ferromagnets, Phys. Rev. B **94**, 144432 (2016).

[26] I. D. Tokman, Q. F. Chen, I. A. Shereshevsky, V. I. Pozdnyakova, I. Oladyshkin, M. Tokman, and A. Belyanin, Inverse faraday effect in graphene and Weyl semimetals, Phys. Rev. B **101**, 174429 (2020).

[27] E. Saitoh, M. Ueda, H. Miyajima, and G. Tatara, Conversion of spin current into charge current at room temperature: Inverse spin-Hall effect, Appl. Phys. Lett. **88**, 182509 (2006).

[28] J. C. R. Sanchez, L. Vila, G. Desfonds, S. Gambarelli, J. P. Attane, J. M. De Teresa, C. Magen, and A. Fert, Spin-to-charge conversion using Rashba coupling at the interface between non-magnetic materials, Nat. Commun. **4**, 2944 (2013).

[29] W. S. M. Werner, K. Glantschnig, and C. Ambrosch-Draxl, Optical constants and inelastic electron-scattering data for 17 elemental metals, J. Phys. Chem. Ref. Data **38**, 1013 (2009).

[30] D. Z. Hou, Z. Qiu, K. Harii, Y. Kajiwara, K. Uchida, Y. Fujikawa, H. Nakayama, T. Yoshino, T. An, K. Ando, X. F. Jin, and E. Saitoh, Interface induced inverse spin hall effect in bismuth/permalloy bilayer, Appl. Phys. Lett. **101**, 042403 (2012).

[31] H. Emoto, Y. Ando, G. Eguchi, R. Ohshima, E. Shikoh, Y. Fuseya, T. Shinjo, and M. Shiraishi, Transport and spin conversion of multicarriers in semimetal bismuth, Phys. Rev. B **93**, 174428 (2016).

[32] Z. Chi, Y.-C. Lau, X. Xu, T. Ohkubo, K. Hono, and M. Hayashi, The spin Hall effect of Bi-Sb alloys driven by thermally excited Dirac-like electrons, Sci. Adv. **6**, eaay2324 (2020).

[33] A. Nomura, T. Tashiro, H. Nakayama, and K. Ando, Temperature dependence of inverse Rashba-Edelstein effect at metallic interface, Appl. Phys. Lett. **106**, 212403 (2015).

[34] S. Karube, K. Kondou, and Y. Otani, Experimental observation of spin-to-charge current conversion at non-magnetic metal/Bi$_2$O$_3$ interfaces, Appl. Phys. Express **9**, 033001 (2016).

[35] A. Hoffmann, Spin Hall effects in metals, IEEE Trans. Magn. **49**, 5172 (2013).

[36] J. Sinova, S. O. Valenzuela, J. Wunderlich, C. H. Back, and T. Jungwirth, Spin Hall effects, Rev. Mod. Phys. **87**, 1213 (2015).

[37] A. Fert and H. Jaffres, Conditions for efficient spin injection from a ferromagnetic metal into a semiconductor, Phys. Rev. B **64**, 184420 (2001).

[38] J. Liu, F. Xia, D. Xiao, F. J. G. de Abajo, and D. Sun, Semimetals for high-performance photodetection, Nat. Mater. **19**, 830 (2020).

[39] E. Togan, Y. Chu, A. S. Trifonov, L. Jiang, J. Maze, L. Childress, M. V. G. Dutt, A. S. Sorensen, P. R. Hemmer, A. S. Zibrov, and M. D. Lukin, Quantum entanglement between an optical photon and a solid-state spin qubit, Nature (London) **466**, 730 (2010).

[40] L. Liu, T. Moriyama, D. C. Ralph, and R. A. Buhrman, Spin-Torque Ferromagnetic Resonance Induced by the Spin Hall Effect, Phys. Rev. Lett. **106**, 036601 (2011).

[41] S. Karimeddiny, J. A. Mittelstaedt, R. A. Buhrman, and D. C. Ralph, Transverse and Longitudinal Spin-Torque Ferromagnetic Resonance for Improved Measurement of Spin-Orbit Torque, Phys. Rev. Appl. **14**, 024024 (2020).

[42] X. Fan, J. Wu, Y. Chen, M. J. Jerry, H. Zhang, and J. Q. Xiao, Observation of the nonlocal spin-orbital effective field, Nat. Commun. **4**, 1799 (2013).